Theunissen, R. (2015). Modelling of imaged ellipse intensity profiles using Euclidean geometry. The Imaging Science Journal, 63(6), 321-331. 10.1179/1743131X15Y.0000000013

Modelling of Imaged Ellipse Intensity Profiles Using Euclidean Geometry

R. Theunissen

Department of Aerospace Engineering, University of Bristol, Queens' Building, University Walk, Clifton, BS81TR, United Kingdom.

r.theunissen@bristol.ac.uk

Abstract

To model the evolution in intensity of an ellipse image along randomly oriented profiles, this paper starts with the derivation of an analytical solution involving infinite summations of products of Hermite polynomials which is consequently argued to be impractical. Generation of profiles adopting Fourier analyses hamper the extraction of arbitrarily located intensity distributions as a direct result of equidistant spatial sampling and an alternative procedure is therefore presented to calculate the sought-for intensity at isolated spatial locations. The algorithm introduced is based on the overlap area between the ellipse and concentric circles which can be performed using basic trigonometric properties. The simplicity of the proposed method allows, contrary to Fourier-based analyses, the modelling of intensity profiles with high resolution while demanding minimal computational memory. The proficiency of the method is demonstrated numerically and its generality and applicability to real images in terms of motion-induced image blurring and digitisation is discussed.

Keywords: Convolution, diffraction, ellipse, FFT, Hermite polynomial, blur.

1. INTRODUCTION

Ellipse detection is recognised as a key problem in image processing and has been consequently the focus of many research papers. Ellipses have a direct application in the field of camera calibration[1,2] and many of the real world problems involving motion tracking can be simplified by decomposing objects into this geometric primitive[3-5]. Although the majority of detection algorithms are based on recorded intensity patterns, be it in terms of Hough transforms[6], intensity gradients[7] or higher order derivatives[8], so far neither an inherent analytical model of the ellipse image nor an easy way of modelling intensity profiles has to the best of the author's knowledge been presented. While analytical models exist for the straight edge-response function[9] involving the error-function, an analytical solution is not as straightforward for curved edges.

As will be shown in the remainder of this paper, the evaluation of derived analytical models quickly becomes computationally ineffective which can be considered a strong argument why the posed problem has received surprisingly limited attention. However, this paper sets out to present a simple approach to model recorded intensity profiles related to the imaging of an ellipse. It is stressed that the objective is to retrieve intensity values at prescribed locations or along randomly distributed profiles with user-defined resolution.

The paper starts with a recapitulation of the imaging process and moves on to the derivation of an analytical model for the ellipse image. After summarizing elementary geometrical properties of the circle-ellipse intersection, a simplification of the posed problem is presented. In particular, it is shown that the convolution operation inherent to the image formation can be described as a weighted summation of overlap areas between circles and the ellipse in question. The validity of the obtained derivations is ascertained by a numerical assessment based on comparison with traditional FFT based methods. The effects of image digitisation and out-of-focus imaging are discussed and shown not to affect the validity or applicability of the proposed method. Finally, the conduciveness of the new routine is ascertained on the basis of an experimental application involving the imaging of ellipses of varying eccentricity at different degrees of focussing. Conclusions finalise the paper.

2. Incoherent Image Formation

The incoherent imaging process yielding the analogue intensity distribution $I_A(x,y)$ is mathematically described as the convolution (symbolised by $*$) between the object $P(X,Y)$ projected onto the image plane and the Point Spread Function $S^{dif}(x,y)$. Coordinates in the object plane are symbolised by (X,Y) and are related to the image coordinates (x,y) by the magnification M.

$$\begin{aligned} I_A(x,y) &= (P * S^{dif})(x,y) \\ &= \int_{-\infty}^{+\infty}\int_{-\infty}^{+\infty} P(\tfrac{x'}{M},\tfrac{y'}{M}) S^{dif}(x-x',y-y')\,dx'\,dy' \end{aligned} \tag{1}$$

The Point Spread Function (PSF) is characteristic of the lens system and takes the form of the Airy irradiance distribution[10] for diffraction-limited incoherent imaging through a circular aperture of diameter D_A, which will be assumed throughout the rest of the paper;

$$S^{dif}(x,y) = S^{dif}(\rho) = 4I_0 \frac{J_1^2(k\rho)}{(k\rho)^2} \tag{2}$$

where $k=D_A\pi/\lambda f$ and $\rho^2=x^2+y^2$. The constant I_0 is a proportionality constant, λ represents the light wavelength, f is the focal length of the lens and $J_n(\cdot)$ is the nth order Bessel function of the first kind. The radial position $\rho_A \approx 1.22\cdot\pi/k$ of the first minimum of $S^{dif}(x,y)$ is generally considered as the Airy disk extent containing approximately 84% of the total incident light energy[11]. A generally accepted simplification is to model the irradiance pattern by a Gaussian[12] with equal value at $\rho=0$;

$$S_m^{dif}(\rho) = I_0 \exp(-\frac{\rho^2}{2w^2}) \tag{3}$$

where $w = \frac{\sqrt{2}}{k}$ and $\rho_A \approx 2.71\cdot w$.

The assumption of a Gaussian-model for the PSF is not limited to ideal optics though. Claxton and Staunton[13] have shown that the PSF of a focused lens subjected to diffraction effects and optical aberrations retains similarity with a Gaussian. Pentland[14] also argues that defocussing can effectively be modelled as a Gaussian shaped PSF. Even considering the top-hat shaped kernel related to motion-blur[15], the Gaussian retains validity as will be shown in the experimental application in section 7. For simplicity the notation S_m^{dif} is kept although it should be noted that in these cases the Gaussian variance w will not be related solely to diffraction. This will not restrict the generality of the proposed methodology as no explicit expression for w is required hereafter.

3. Analytic Incoherent Ellipse Image

In this paragraph an analytical expression describing the intensity distribution related to the imaged ellipse with incoherent point sources is deducted. The projection of an ellipse onto the image plane will remain elliptical with semi-axes a and b. Without loss of generality, the projection is assumed to be centred on the origin of the image coordinate system (x,y) allowing the object image $P(x,y)$ to be defined as

$$P(x,y) = \begin{cases} 1 & \frac{x^2}{a^2} + \frac{y^2}{b^2} \le 1 \\ 0 & \text{else} \end{cases} \tag{4}$$

A convolution in space *(x,y)* can be rewritten as a multiplication in the spectral domain *(u,v)*, by which the exact expression (1) is transformed into Fourier constituents;

$$I_A(x,y) = \frac{1}{2\pi} \int_{-\infty}^{+\infty} \int_{-\infty}^{+\infty} \Im\{P\}\Im\{S^{dif}\} \exp(i(xu+yv)) du dv \tag{5}$$

where the Fourier transform of the ellipse equals

$$\Im\{P(x,y)\}(u,v) = ab\frac{J_1(\tau)}{\tau} \tag{6}$$

and $\tau = \sqrt{(au)^2 + (bv)^2}$. The Fourier transform of the PSF defined in (2), i.e. the Optical Transfer Function (OTF) of the lens, can be determined as the auto-correlation of the scaled lens' pupil function

$$\begin{aligned} &\Im\{S^{dif}(x,y)\}(u,v) = OTF(u,v) \\ &= I_0 \tfrac{2}{\pi}[\arccos(\pi \tfrac{u^2+v^2}{k}) - \pi \tfrac{u^2+v^2}{k}\sqrt{1-\pi^2 \tfrac{(u^2+v^2)^2}{k^2}}] \end{aligned} \tag{7}$$

The modelled irradiance pattern allows on the other hand a more manageable expression

$$\Im\{S_m^{dif}(x,y)\}(u,v) = I_0 w^2 \exp(-\tfrac{w^2}{2}(u^2+v^2)) \tag{8}$$

Combining (6) and (8) into (5)

$$\begin{aligned} I_{A,m}(x,y) = \tfrac{abI_0w^2}{2\pi} \int_{-\infty-\infty}^{+\infty+\infty} \tfrac{J_1(\sqrt{(au)^2+(bv)^2})}{\sqrt{(au)^2+(bv)^2}} \\ \times \exp(-\tfrac{w^2(u^2+v^2)}{2}) \exp(i(xu+yv)) du dv \end{aligned} \tag{9}$$

The double integral in (9) can be further simplified by writing the Bessel function as a summation

$$\frac{J_1(x)}{x} = \frac{1}{2}\sum_{m=0}^{+\infty} \frac{(-1)^m}{4^m m!(m+1)!} x^{2m} \tag{10}$$

using the identity

$$\Im\{x^n f(x)\}(u) = i^n \frac{d^n}{du^n}\Im\{f(x)\}(u) \tag{11}$$

and defining the nth degree Hermite polynomial $H_n(x)$ as

$$H_n(x) = (-1)^n \exp(x^2)\frac{d^n}{dx^n}\exp(-x^2) \tag{12}$$

resulting in

$$I_{A,m}(x,y) = \frac{abI_0}{2}\exp\left(-\frac{x^2+y^2}{2w^2}\right)\sum_{p=0}^{+\infty}\frac{1}{4^p\,p!}\left(\frac{b}{\sqrt{2}w}\right)^{2p}H_{2p}\left(\frac{y}{\sqrt{2}w}\right) \times\sum_{q=0}^{+\infty}\frac{1}{4^q\,q!(q+p+1)!}\left(\frac{a}{\sqrt{2}w}\right)^{2q}H_{2q}\left(\frac{x}{\sqrt{2}w}\right) \tag{13}$$

Equation (13) provides an analytical expression of the intensity distribution inherent to the incoherent imaging of an ellipse assuming a Gaussian shaped OTF of the lens system. From a practical perspective, accurate numerical evaluation of (13) is neigh impossible due to the double infinite summation of Hermite polynomials. According Boyd[16] $H_n(x)$ is bounded by $(n!)^{1/2}\cdot\exp(\tfrac{1}{2}x^2)$ indicative that the importance of the terms in the summation in (13) grows with n and that consequently all terms must be considered making the procedure computationally expensive. In addition, with increasing argument or polynomial degree accuracy will decrease as a result of limited machine precision.

Evaluation of (1) or (9) can alternatively be performed by means of routines based on Fast Fourier Transforms[17] (FFT) as per equation (5). In this case pseudo-images of P and S_m^{dif} are generated at a certain resolution, Fourier transformed, multiplied and the result is transformed back into the spatial domain. Because of finite computer memory the potential number of spatial samples and extent of the spatial domain (i.e. size of the pseudo-images) will be limited. Both Fourier transforms in (6) and (8) have infinite spectral extent however. The accompanying truncation in frequency domain and the under-resolved spectra will inevitably introduce aliasing artefacts and reconstruction errors. A similar reasoning applies to the re-transformation of (9) to coordinate space. Such inaccuracies will be independent of elliptic eccentricity and especially prominent for small ellipse radii or small w. Moreover, the 2D intensity distributions obtained through FFT analyses are only defined at discrete, regular spaced locations. If the interest lies in well-resolved 1D intensity profiles along arbitrary direction, FFT will become too memory consuming due the needed increased sampling and consequently inefficient. This will be demonstrated by a numerical example in section 5. For this reason, a simple method to calculate the intensity at a single spatial location is presented in the following, allowing the calculation of intensity profiles along any direction at a predefined resolution.

4. Geometric Interpretation of Convolution

4.1 Principle

In the following an alternative to (9) and (13) is suggested focusing on increasing resolution in intensity profiles while limiting computational effort. The approach is inspired by Verbeek and van Vliet[18] where the accuracy of higher order derivative based edge detection methodologies is assessed. The fundamental principle is the equivalence between the convolution $(P*C)(x,y)$ and the overlap area $A(x_c,y_c,l)$ between the ellipse image (4) and circle $C(x_c,y_c,l)$

$$C(x_c,y_c,l)=\begin{cases}1 & (\mathrm{x}-\mathrm{x_c})^2+(\mathrm{y}-\mathrm{y_c})^2\le \mathrm{l}\\ 0 & \text{else}\end{cases} \tag{14}$$

The concept is accordingly to represent the normal distributed irradiance $S_m^{dif}(l)$ as a stack of concentric pillboxes of height dS_m^{dif} and monotonic radius distribution $l(S_m^{dif})$, allowing the convolution $(P*S_m^{dif})(x,y)$ to be expressed as a summation of overlap areas for circles of different radii (Fig. 1);

$$\begin{aligned} I_{A,m}(x_c,y_c) &= \lim_{l\to+\infty}\int_{S_m^{dif}(l)}^{S_m^{dif}(0)} A(x_c,y_c,l(S_m^{dif}))dS_m^{dif} \\ &= -\int_0^{+\infty} A(x_c,y_c,l)\frac{dS_m^{dif}}{dl}dl \end{aligned} \tag{15}$$

As an example, in case of a straight edge defined as $P(x,y)=0$ for $x>0$ and $P(x,y)=1$ if $x\le 0$, the overlap with a circle of radius l centred on (x_c,y_c) is readily given as

$$A(x_c,y_c,l)=l^2\arccos(x_c/l)-x_c\sqrt{l^2-x_c^{\,2}} \tag{16}$$

which after substitution of (16) and $dS_m^{dif}/dl=-l/w^2\cdot exp(-l^2/2w^2)$ in (15) yields the well-known edge spread function involving the complementary error function[9];

$$I_{A,m}(x_c,y_c)=\pi w^2 I_0 erfc\left(\frac{x_c}{\sqrt{2}w}\right) \tag{17}$$

4.2 Ellipse Edge

In case of an object with continuous variation in curvature, such as an ellipse, there exist at least two radii, $l_{t,min}$ and $l_{t,max}$ (Fig. 2), for any position (x_c,y_c) such that the corresponding concentric circles will have exactly one tangent point with the ellipse. The integral bound in (15) can accordingly be partitioned and with $S_m^{dif}(x,y)$ as defined in (3) follows

$$I_{A,m}(x_c,y_c)=\overbrace{\begin{cases}2\pi w^2 I_0\gamma(2,\frac{l_{t,\min}^2}{2w^2}) & \rho_c\le\rho_e(\theta)\\ 0 & \text{else}\end{cases}}^{T_1;\quad 0\le l\le l_{t,\min}}$$
$$+\overbrace{\frac{I_0}{w^2}\int_{l_{t,\min}}^{l_{t,\max}}A(x_c,y_c,l)\,l\exp(-\frac{l^2}{2w^2})dl}^{T_2;\quad l_{t,\min}\le l\le l_{t,\max}}$$
$$+\overbrace{\pi ab\cdot I_0\exp(-\frac{l_{t,\max}^2}{2w^2})}^{T_3;\quad l_{t,\max}\le l\le+\infty} \tag{18}$$

Equation (18) is graphically presented in Fig. 1 with the individual terms T_1, T_2 and T_3 indicated.

In (18), ρ_c is the radial position of the circle with respect to the ellipse and $\rho_e(\theta)$ is the ellipse radius along the angle θ;

$$\rho_c=\sqrt{x_c^2+y_c^2}\ ,\ \rho_e(\theta)=\frac{ab}{\sqrt{b^2\cos^2(\theta)+a^2\sin^2(\theta)}} \tag{19}$$

with $\theta=arctan(y_c,x_c)$. The incomplete gamma function $\gamma(a,x)$ in T_1 is given by

$$\gamma(a,x)=\int_0^x t^{a-1}\exp(-t)dt \tag{20}$$

For sufficiently large $l_{t,max}$ T_3 equals zero. For this reason a radius l_ε can be introduced for which $|dS_m^{dif}(l)/dl|=\varepsilon$;

$$l_\varepsilon=\sqrt{2}w\sqrt{-\tfrac{1}{2}W_{-1}(-\varepsilon^2w^2)} \tag{21}$$

where $W_{-1}(\cdot)$ is the -1-branch of Lambert's W function and ε approaches zero ($\varepsilon\approx10^{-20}$). Combining (21) and (18) then allows a further simplification;

$$I_{A,m}(x_c,y_c)=\begin{cases}2\pi w^2 I_0\gamma(2,\frac{l_{t,\min}^2}{2w^2}) & \rho_c\le\rho_e(\theta)\\ 0 & \text{else}\end{cases}$$
$$+\frac{2I_0}{w^2}\int_{l_{t,\min}}^{\min(l_\varepsilon,l_{t,\max})}A(x_c,y_c,l)\,l\exp(-\frac{l^2}{2w^2})dl$$
$$+\begin{cases}\pi ab\cdot I_0\exp(-\frac{l_{t,\max}^2}{2w^2})) & l_{t,\max}\le l_\varepsilon\\ 0 & \text{else}\end{cases} \tag{22}$$

Comparison between (1), (9) and (22) reveals that the double integral is reduced to a single integration in radial direction where $l_{t,min}$, $l_{t,max}$ and $A(x_c,y_c,l)$ are still to be determined. While terms T_1 and T_3 in (18) and (22) are exact expressions, T_2 must be approximated by conventional numerical integration techniques. Currently the Simpson's Rule approximation is incorporated yielding evaluation errors in the order of $O(dl^4)$ with $dl=[min(l_\varepsilon, lt_{,max})-l_{t,min}]/N$ and N typically 10^3.

Note that by repeating the above procedure for ellipses with semi-axes $a+\delta t$, $b+\delta t$ and $a-\delta t$, $b-\delta t$ and subtracting the obtained intensity distributions, the intensity profile across an ellipse-shaped line of thickness $2\cdot\delta t$ can be obtained.

4.3 Tangent Circles

Given a circle location (x_c,y_c), the approach of Emiris and Tzoumas[19] allows the calculation of the tangent circle radii l_t as the roots of the quartic polynomial $\sum_{q=0}^{4} c_{0q} l_t^{q/2} = 0$. The coefficients c_{0q} are defined as

$$\begin{aligned}
c_{00} &= \xi_3^2(\xi_4^2 + 4\xi_2^2\xi_3)\\
c_{01} &= 2(2\xi_4^3 - \xi_1\xi_3\xi_4^2 - 6\xi_1\xi_2^2\xi_3^2 + 9\xi_2^2\xi_3\xi_4 - \xi_2\xi_3^2\xi_4)\\
c_{02} &= -18\xi_2^3\xi_3 + 4\xi_1\xi_2\xi_3\xi_4 - 27\xi_2^4 + \xi_1^2\xi_4^2\\
&\quad -18\xi_1\xi_2^2\xi_4 + \xi_2^2\xi_3^2 + 12\xi_1^2\xi_2^2\xi_3 - 12\xi_2\xi_4^2\\
c_{03} &= 2\xi_2(9\xi_1\xi_2^2 - \xi_1^2\xi_4 + 6\xi_2\xi_4 - 2\xi_1^3\xi_2 - \xi_1\xi_2\xi_3)\\
c_{04} &= \xi_2^2(\xi_1^2 - 4\xi_2)
\end{aligned} \tag{23}$$

where $\xi_1=a^2+b^2$, $\xi_2=a^2b^2$, $\xi_3=b^2x_c^2+a^2y_c^2-\xi_2$ and $\xi_4=\xi_2(x_c^2+y_c^2-\xi_1)$. The maximum and minimum in the obtained l_t values then represent $l_{t,max}$ and $l_{t,min}$ respectively.

4.4 Circle Ellipse Overlap

For any radius $l_{t,min}\leq l\leq l_{t,max}$ the intersection between a circle and ellipse centred on C and O respectively yields either two or four instances (Fig. 2). The x and y coordinates of the intersection points readily follow as the roots of two quartic polynomials[20] obtained by simultaneously solving (4) and (14) for either coordinate. Note that in case of a tangent point, two of the four roots will be identical. The overlap area $A(x_c,y_c,l)$ can now be defined based on simple Euclidean trigonometry.

The straightforward calculation of the overlap area in case of two intersection points $P_1(x_1,y_1)$ and $P_2(x_2,y_2)$ where $\theta_1\leq\theta_2$ and $\theta_i\in[0,2\pi]$ consists of the sum of the circular arc segment area A_{12}^c and the elliptical segment area A_{12}^e subtracted by triangular area A_{12}^t. The individual area contributions are readily given by

$$A_{12}^c = \frac{l^2}{2}(\alpha - \sin(\alpha)) \tag{24}$$

where $\alpha = \pi - \arccos\left(\frac{\sqrt{(x_2-x_1)^2+(y_2-y_1)^2}}{2l}\right)$ $\quad A_{12}^t = \frac{1}{2}\,|\,x_1y_2 - x_2y_1\,|$ (25)

$$A_{12}^{e} = \frac{ab}{2}(\varphi_2 - \varphi_1) \tag{26}$$

with $\varphi_i = \arctan(\frac{a}{b}\tan(\theta_i))$ and $\varphi_i \in [0,2\pi]$. Depending on the relative positions of the points P_i and ellipse/circle origins the variation in area contributions defined above must be accounted for. Firstly, the limiting angle β_{lim} and radius l_{lim} are introduced symbolizing the maximum angle spanned between vectors OP_1 and P_1C and corresponding radius respectively. Note that l_{lim} represents the circle radius for which the intersection points are collinear with O.

$$l_{\lim}^2 = (\frac{ab}{\kappa} y_c - x_c)^2 + (\frac{ab}{\kappa} x_c + y_c)^2 \tag{27}$$

with $\kappa^2 = a^2 x_c^2 + b^2 y_c^2$

$$\beta_{\lim} = \arcsin(\frac{\rho_c}{l_{\lim}}) \tag{28}$$

The actual angle is denoted by β and evaluated as

$$\beta = \arccos(\frac{x_1(x_1 - x_c) + y_1(y_1 - y_c)}{\rho_e(\theta_1)\cdot\rho_c}) \tag{29}$$

Equations (20)-(25) are combined into a single parameter ω defined as

$$\omega = \begin{cases} 1 & \beta \le \beta_{\lim} \text{ and } l_{\lim} \le \rho_c \\ 0 & \text{else} \end{cases} \tag{30}$$

Next, parameter ψ relating the relative linear distances from the midpoint of vector P_1P_2, (x_m,y_m), through C to the ellipse and circle is defined as

$$\psi = \begin{cases} 1 & \lambda_c \le \lambda_e \\ 0 & \text{else} \end{cases} \tag{31}$$

with $\lambda_c = 1 + (\sqrt{\delta_x^2 + \delta_y^2})^{-1}$, $\delta_x = x_c - x_m$ and $\delta_y = y_c - y_m$. Variable λ_e is the largest real root of the second order polynomial $c_{20} + c_{21}\lambda_e + c_{22}\lambda_e^2 = 0$ with coefficients $c_{20} = (x_m/a)^2 + (y_m/b)^2 - 1$, $c_{21} = (2x_m\delta_x/a^2) + (2y_m\delta_y/b^2)$ and $c_{22} = (\delta_x/a)^2 + (\delta_y/b)^2$. Finally, the general expression for the overlap area $A(x_c,y_c,l)$ in case of two intersection points is given by

$$\begin{aligned} A(x_c, y_c, l) = &\{\psi\pi l^2 + (1-2\psi)A_{12}^{c}\} \\ &+ \{\omega\frac{\pi ab}{2} + (1-2\omega)A_{12}^{e}\} - \{(1-2\omega)A_{12}^{t}\} \end{aligned} \tag{32}$$

For the case of four intersection points, derivations in the following assume the sequence of corner points P_i to be arranged according increasing angle θ_i and to be cyclic i.e. $P_{4+i} = P_i$. The area of the trapezoid defined by the points P_i consists of the combined area of the individual triangles $P_1P_2P_3$ and $P_1P_3P_4$ (Fig. 2). For each side of the trapezoid, arc segments and triangular areas are calculated applying equations

(24) to (26). Similar to the previous case additional parameters are needed to evaluate the relative point positions. Let $\chi_i=arctan(y_i-y_c/x_i-x_c)$ denote the angle of point P_i with respect to the circle centre C with $\chi_i \in [0,2\pi]$ and define ω_i as 1 if $\chi_{i+1}-\chi_i > \pi$ or 0 else. Let $\delta_{xi}=x_{mi}-x_{mi+2}$, $\delta_{yi}=y_{mi}-y_{mi+2}$, $\mu_{xi}=x_{mi+2}-x_c$ and $\mu_{yi}=y_{mi+2}-y_c$ with midpoint coordinates $x_{mi}=½(x_i+x_{i+1})$ and $y_{mi}=½(y_i+y_{i+1})$. Parameters λ_{ci} and λ_{ei} are then the largest real roots of the polynomials $c_{30}^i + c_{31}^i\lambda_{ci} + c_{32}^i\lambda_{ci}^2 = 0$ and $c_{40}^i + c_{41}^i\lambda_{ei} + c_{42}^i\lambda_{ei}^2 = 0$ respectively defined by the coefficients $c_{30}{}^i=\mu_{xi}{}^2+\mu_{yi}{}^2-l^2$, $c_{31}{}^i=2\mu_{xi}\delta_{xi}+2\mu_{yi}\delta_{yi}$, $c_{32}{}^i=\delta_{xi}{}^2+\delta_{yi}{}^2$, $c_{40}{}^i=b^2x_{mi+2}{}^2+a^2y_{mi+2}{}^2-a^2b^2$, $c_{41}{}^i=2b^2x_{mi+2}\delta_{xi}+2a^2y_{mi+2}\delta_{yi}$ and $c_{42}{}^i=b^2\delta_{xi}{}^2+a^2\delta_{yi}{}^2$. The obtained roots are combined in parameter ψ_i, which equals 1 provided $\lambda_{ei} \leq \lambda_{ci}$ or 0 else.

The overlap area between the circle and ellipse in case of four intersection points is then given as

$$A(x_c, y_c, l) = \{A_{123}^t + A_{134}^t\} + \sum_{i=1}^{4} (1-\psi_i)\{\omega_i \pi l^2 + (1-2\omega_i)A_{ii+1}^c\} + \psi_i\{A_{ii+1}^e - A_{ii+1}^t\} \quad (33)$$

4.5 Implementation

The stepwise algorithm is presented in pseudo code below, substantiating the advocated simplicity. Only inputs consist of the point location (x_c,y_c) of interest, ellipse semi-major axes a and b and the standard deviation w of the PSF S_m^{diff}. The author would like to emphasise that the implementation below is by no means restricted to ideal imaging or continuous images. The only assumption is the PSF to follow a normal distribution, which has been argued in section 2 to be a valid generalisation. No definition of w is required. The choice of (x_c,y_c) is free and can be selected to coincide with discrete instances as in digital images. Subsequent calculations are performed in continuous space but are unrelated to the image type and only reflect the continuous nature of the real-world imaging process. Consequently, image properties such as digitisation level and image size will not affect the method.

calculate $l_{t,min}$, $l_{t,max}$, l_ε, l_{lim}, β_{lim}, $\rho_e(\theta)$, ρ_c, T_1, T_3

initialise $n=0$

for l from $l_{t,min}$ to $l_{t,max}$

calculate dS_m^{diff}/dl

update $n=n+1$

solve quartic to calculate intersection points P_i between (4) and (14)

sort P_i according increasing θ_i

if #P_i=2

calculate $\rho_e(\theta_1)$, β, ω, λ_c, λ_e, ψ, A_{12}^c, A_{12}^t, A_{12}^e, A

update $T(n)=A \cdot dS_m^{dif}/dl$

elseif #P_i=4

calculate A_{123}^t, A_{134}^t

for i from 1 to 4

calculate χ_i, ω_i, λ_{ci}, λ_{ei}, ψ_i, A_{ii+1}^c, A_{ii+1}^t, A_{ii+1}^e

end

calculate A

update $T(n)=A \cdot dS_m^{dif}/dl$

end

end

calculate T_2 using T (numerical integration)

calculate $I_{A,m}(x_c,y_c) = T_1+T_2+T_3$

5. Numerical Assessment

A generic example is presented in Fig.3 where the radial intensity profile across the ellipse semi-major axis is depicted based on (9), i.e. adopting Fast Fourier Transforms. To avoid errors due to truncation of the PSF, the spatial domain considered extended from the ellipse boundaries by ten diffraction diameters and sampled by N_{FFT} points. Obtained results are consequently representative for a constant frequency resolution but increasing sampling frequency $f_s=N_{FFT} \cdot [2 \cdot a \cdot (1+10 \cdot w)]^{-1}$(read spectral extent). The author would like to emphasise that intensity profiles along angles different from multiples of $\pi/4$ radians are impossible to obtain directly from FFT analyses due to the mismatch between the extraction line and original equidistant (pixel-) samples. The exact solution is represented by the proposed method where calculations are performed by dividing the considered domain $[a-10 \cdot w, a+10 \cdot w]$ into 10^3 sections.

With increasing sampling frequency the discretisation and edge localisation of the intensity profile based on FFT analyses improves. Obtained results tend to the exact solution (solid line) only asymptotically proving the proposed method to be correct. The figure further substantiates poor sampling to lead to poor edge representations and erroneous edge localisation. Fig.3 further indicates an evident discrepancy between edge spread functions (ESF) across curved and straight edged objects (dotted line). It is well known that as a direct result of the local curvature of the imaged object a bias will be introduced in the edge localisation towards the centre of the ellipse. This is visible as a shift between the ESFs.

Provided sampling is adequate, the maximum discrepancy ε_{max} between the exact and FFT-based profiles depicted in Fig.4, is indicative of the degree of accuracy. As expected, discrepancies tend to decrease with increasing number of points considered in the FFT analyses and increasing normalised diffraction spot diameter w/a.

Regarding computational effort, the pseudo code was implemented on a desktop PC (dual-core @2.67GHz, 4Gb RAM) in the commercial software package Matlab without further efforts to optimise the computational speed. Integrals were calculated adopting Simpson's rule utilising 10^3 intermediate steps. The resulting computation time amounted to 0.2 seconds per sampling point and was partitioned in the solution of the quartic equation (4%), evaluation of the Lambert function W_{-1} (25%) and the calculation of the overlap areas (65%). The ratio in computation time between the FFT-based methodology (t_{FFT}) and proposed method ($t_{current}$) is depicted in Fig.5 as a function of N_{FFT}, imposing identical number of points across the methods to equal the spatial resolution. For $N_{FFT} \leq 2^{12}$ the ratio increases quasi-linearly implying the traditional method to be more computationally efficient as can be expected from the use of Fast Fourier Transforms. However, the poorer sampling drastically compromises the accuracy of the FFT-based method (Fig.4) whereas the convolution-based algorithm safeguards accuracy independent of N_{FFT}. The concomitant requirement that images are N_{FFT}^2 pixels^2 in size increases memory usage and may become sufficiently restrictive to favour the new method. Fig.5 effectively indicates that for $N_{FFT}=8192$ the proposed method offers a gain in speed by a factor 10. This is an important finding. First the current technique takes the spatial distance between the profile points as an input and is therefore the method of choice when well-resolved profiles are needed. Second, the convolution based

calculation of the intensity profile may be more intense when requiring less spatial resolution but, contrary to the traditional methodology, does not compromise accuracy. Third, increasing computing power will not aid the conventional models but would instead make the proposed technique even more attractive given its computational simplicity. Even with enhanced computational performance, analyses invoking FFT cannot extract intensity profiles along random directions, contrary to the proposed method.

6. Generalisation: Image Blur and Digitisation

The PSF can be accurately modelled as a Gaussian even in the presence of lens aberrations and out-of-focus imaging, In the following it will be argued that the above modelling methodology can be easily adopted to include image blur due to motion and pixelisation effects.

The PSF S^{mb} in case of motion blur can be represented again as a pillbox of diameter D_b [15] which, following the previous analyses and noting that the result must remain axi-symmetric yields the combined response of the blurring system S_m^c;

$$\begin{aligned} S_m^c(x,y) &= S^{mb} * S_m^{dif} \underset{\substack{x=\rho\cos(\theta)\\ y=\rho\sin(\theta)}}{\overset{\substack{u=\tau\cos(\eta)\\ v=\tau\sin(\eta)}}{=}} S_m^c(\rho) \\ &= \pi D_b I_0 \int_{-\infty-\infty}^{+\infty+\infty} \frac{J_1(\frac{D_b}{2}\sqrt{u^2+v^2})}{\sqrt{u^2+v^2}} \exp(-\frac{w^2(u^2+v^2)}{2}) \\ &\quad \times \exp(i(ux+vy))dudv \\ &= 4\pi^2 I_0 \int_0^{+\infty} \frac{1}{\tau} J_1(\frac{D_b\tau}{2}) J_o(\rho\tau) \exp(-\frac{\tau^2 w^2}{2}) d\tau \end{aligned} \tag{34}$$

Because the combined PSF S_m^c is a monotonic function in radius l, equation (18) can still be used to calculate the imaged ellipse with the following substitutions

$$\frac{dS_m^c(l)}{dl} = -4\pi^2 I_0 \int_0^{+\infty} J_1(\frac{D_b\tau}{2}) J_1(l\tau) \exp(-\frac{\tau^2 w^2}{2}) d\tau \tag{35}$$

$$T_3 = 4\pi^3 abI_0 \int_0^{+\infty} \frac{1}{\tau} J_1(\frac{D_b\tau}{2}) J_o(l_{t,\max}\tau) \exp(-\frac{\tau^2 w^2}{2}) d\tau \tag{36}$$

$$T_1 = 4\pi^3 l_{t,\min}^2 I_0 \int_0^{+\infty} \frac{1}{\tau} J_1(\frac{D_b}{2}\tau) J_2(l_{t,\min}\tau) \exp(-\frac{\tau^2 w^2}{2}) d\tau \tag{37}$$

Equation (37) is valid provided $\rho_c \leq \rho_e$ or $T_1=0$ otherwise. Because of missing explicit analytical solutions[21], the infinite integrals (34)-(37) can only be evaluated

numerically by means of efficient algorithms[22]. Consideration of motion-induced blur with the presented methodology is consequently feasible though computationally more intense than conventional imaging (including blur and lens aberrations).

The continuous image intensity distribution $I_A(x,y)$ is commonly discretised with an electronic imaging device (typically a CCD camera), integrating the light intensity over small sensor areas referred to as pixels. The pixels are characterised by their size Δ and the relative fraction p^2 of the total pixel area that is light sensitive[23]. The generated electronic charge, and therefore the recorded light intensity, is assumed to be directly proportional to the incident light intensity. The digitisation can be represented as a convolution of $I_A(x,y)$ with the pixel-dependent sampling function $\phi(x,y)$ followed by discretisation with the Dirac function $\delta(s\Delta,t\Delta)$. With (1) and using the associative property of the convolution operator the digitisation process can be reformulated still involving a continuous diffraction-related PSF

$$\begin{aligned} I_{D,m}(s\Delta,t\Delta) &= (I_{A,m} * \phi)(x,y) * \delta(s\Delta,t\Delta) \\ &= (P * (S_m^{dif} * \phi))(x,y) * \delta(s\Delta,t\Delta) \\ &= (P * S_{m,D}^{dif})(x,y) * \delta(s\Delta,t\Delta) \end{aligned} \tag{38}$$

where

$$\phi(x,y) = \begin{cases} \Delta^{-2} & |x| < \frac{1}{2}\Delta, |y| < \frac{1}{2}\Delta \\ 0 & \text{else} \end{cases} \tag{39}$$

and

$$\begin{aligned} S_{m,D}^{dif}(x,y) = \frac{\pi w^2 I_0}{2p^2\Delta^2} &[erf(\tfrac{\zeta}{\sqrt{2}}\{x_n + \tfrac{1}{2}\}) - erf(\tfrac{\zeta}{\sqrt{2}}\{x_n - \tfrac{1}{2}\})] \\ \times &[erf(\tfrac{\zeta}{\sqrt{2}}\{y_n + \tfrac{1}{2}\}) - erf(\tfrac{\zeta}{\sqrt{2}}\{y_n - \tfrac{1}{2}\})] \end{aligned} \tag{40}$$

where $(x_n,y_n)=(x/p\Delta,y/p\Delta)$, $\zeta=p\Delta/w$ and *erf* is the error function. The maximum variation in normalised $S_{m,D}^{dif}(\rho,\theta)$ with respect to the angular mean $\mu_S(\rho)$ as a function of ζ^{-1} is depicted in Fig.5(a). Fig.5(b) presents the random mean square (rms_{fit}) and mean error (ε_{fit}) between the angular mean $\mu_S(\rho)$ and its Gaussian fit with variance σ_{fit}^2. The figures indicate angular variations in $S_{m,D}^{dif}$ to decrease with increasing $w/p\Delta$ ratio and to be marginal overall. Together with σ_{fit}/w deviating only slightly from unity for $w/p\Delta>1$, $S_{m,D}^{dif}(\rho,\theta)$ can be assumed axi-symmetric and be well approximated by the original irradiance distribution $S_m^{dif}(\rho)$. The proposed method to derive intensity profiles is thus argued to retain its validity in case of digital images provided diffraction disk diameters are in excess of approximately

one pixel. The applicability of the presented technique is thus ensured considering the tendency of decreasing physical pixel size in digital camera development. Discretisation consequently only implies the evaluation of the convolution between object $P(x,y)$ and modified PSF at discrete spatial (i.e. pixel) locations as indicated by (38).

7. Experiment

An experiment was performed to test the validity of the proposed modelling technique. Images of ellipses of varying eccentricity (a=70mm, b/a=0.071 and b/a=0.286) were recorded by means of a standard Canon EOS 10D digital camera (3072×2048pix^2, 24 bit depth, Δ=7.38μm) equipped with a fixed 28mm focal length lens and f-stop set at 5.6. By increasing the distance between the camera and ellipse blur due to out-of-plane focus was varied. In the following, once focused the distance was increased by a factor 1.33 (Fig.7(a)). The variance of the PSF, i.e. w, was in each case derived by fitting the intensity profiles across the rectangular blocks with the analytical edge spread function defined in (17) as illustrated in Fig.7(b). These rectangles further allowed the determination of the conversion factor between millimetre and pixels. Radial intensity profiles for the ellipses were extracted along the major semi-axis using quintic B-spline interpolation[24] to enable comparison with the conventional method. FFT analyses were performed using N_{FFT}=2048 yielding an normalised resolution $\Delta x/w=2\cdot(a/w+1)\cdot N_{FFT}^{-1}$.

Fig.8(a-d) compares the measured and calculated normalised intensity profiles, $I_{norm}=(I-I_{min})\cdot(I_{max}-I_{min})^{-1}$, for varying imaging conditions and the theoretical Edge Spread Function (17). For the larger in-focus ellipse (w/a=2.13·10^{-3}, b/a=0.286) both the ESF and current method provide a profile corresponding to the real image, whereas a discrepancy can be observed with the FFT method as per the numerical example in section 5 (Fig.4). In addition the FFT-based method yields an edge profile with a spatial resolution approximately equal to that of the original image (Fig.8(a)). The current method on the other hand yields a resolution $\Delta x/w$=20/10^3, equalled by the FFT-based method for N_{FFT}=35065. This would impose a severe penalty on memory usage (cf. Fig.5). Consequently, the proposed method based on convolution provides a more accurate basis for edge localisation. A similar conclusion can be drawn for the more eccentric ellipse (Fig.8(b)), where it can be noted that neither the ESF nor the FFT-based date coincide with the current method,

although the latter continues to follow the real-life intensities. Increasing the distance between the object and camera (without re-focussing) widens the ESF. The blurred ellipse edge concomitantly becomes better resolved by the FFT-based method and discrepancies with the current method become marginal. Both methodologies agree with the real intensity distribution (Fig.8(c)). The ESF on the other hand becomes less suitable as a model, which is clearly visible when increasing the eccentricity of the ellipse (Fig.8(d)). These findings support the conclusions drawn from the numerical assessment. Furthermore, for in-focus images *w* amounted to approximately 2.5 pixels, thus allowing the PSF due to pixelisation to be well approximated by the normally distributed PSF as suggested in section 6. The current experiments corroborate this supposition since the proposed method is shown to provide intensity profiles in very close agreement with those obtained from the digital images.

8. Conclusion

In this paper an analytic expression is derived describing the intensity of an imaged ellipse. Because the solution to the mathematical model is impractical to evaluate one must resort to numerical techniques. Routines based on FFT analyses to predict intensity profiles only provide intensity values at discrete, regularly spaced intervals and are therefore inappropriate to model randomly oriented intensity profiles. An alternative method to calculate the image intensity at a particular point is presented in this paper, modelling the Point Spread Function by a Gaussian. The proposed technique involves the stepwise application of basic Euclidian trigonometry, advocating its simplicity. This method allows the prediction of image intensities along any line with predefined spatial resolutions previously impossible to obtain from FFT-based analyses due to involved memory costs.

Numerical assessment has indicated the advantages of the routine with respect to FFT analyses in terms of accuracy and resolution, especially for small diffraction spot diameters. While the described methodology considered a continuous Point Spread Function, the method is argued to retain its validity in case of pixelisation effects in digital images provided diffraction disk diameters are in excess of approximately one pixel. This has further been supported by experiments. It is in addition shown that the technique can be easily extended to incorporate motion-induced image blur.

Experiments have further shown the proposed method to consistently yield intensity profiles across the ellipse edge nearly identical to those recorded by a digital camera, contrary to the analytical Edge Spread Function. Unlike the FFT-based method the current routine does not compromise between accuracy and computational effort.

Overall, the method is thought to be an effective alternative tool in image processing as it enables the accurate modelling of ellipse images allowing more accurate evaluations of intensity profiles and hence intensity or derivative based edge detection schemes.

Because the fundamental concept is to represent the PSF as a series of pillboxes, the proposed method can be extended to incorporate geometric features other than ellipses. In this case only a redefinition of the overlap areas is required. This is part of future work.

References

[1] Heikkila, J., Moment and curvature preserving technique for accurate ellipse boundary detection. Proc. Fourteenth Int. Conf. on Pattern Recognition, 16-20 August 1998, 734-737

[2] Willert, C.E., Assessment of camera models for use in planar velocimetry calibration, Exp. Fluids, 2006, **41**,135-143

[3] Birchfield, S., Elliptical head tracking using intensity gradients and color histograms, IEEE Proc. of Computer Society Conference on Computer Vision and Pattern Recognition, 23-25 June 1998, 232-237

[4] Ruan, D., Fessler, J.A. and Balter J.M., Mean position tracking of respiratory motion, Med. Phys., 2008, **32**, 2, 782-792

[5] Usabiaga, J., Erol, A., Bebis, G., Boyle, R. and Twombly, X., Global hand pose estimation by multiple camera ellipse tracking, Mach. Vision Appl., 2009, **21**, 1-15

[6] Chia, A.Y.S., Leung, M.K.H., Eng, H-L. and Rahardja, S., Ellipse detection with Hough transform in one dimensional parametric space, IEEE Int. Conf. Image Processing, ICIP 2007, Sept. 16-Oct. 19 2007, **5**, 333-336,

[7] Heikkila, J., Geometric camera calibration using circular control points, IEEE Transactions on Pattern Analysis and Machine Intelligence, 2000, **22**, 10, 1066-1077

[8] Haralick, R.M., Digital step edges from zero crossing of second directional derivatives, IEEE T. Pattern Anal., **PAMI-6**, 1984, 58-68

[9] Johnson, C.B., Point-Spread Functions, Line-Spread Functions and Edge-Response Functions Associated with MTFs of the Form exp[-(ω/ωr)n], Appl. Optics, 1973, **12**, 5, 1031-1033

[10] Hecht, E., Optics, 2002, Addison Wesley

[11] Born, M., and Wolf, E., Principles of Optics: Electromagnetic Theory of Propagation, Interference and Diffraction of Light, 1980, Cambridge University Press

[12] Mahajan, V.N., Abberated point-spread functions for rotationally symmetric aberrations, Appl. Optics, 1983, **22**, 19, 3035-3041

[13] Claxton, C.D., and Staunton, R.C., Measurement of the point-spread function of a noisy imaging system, J. Opt. Soc. Am. A, 2008, **25**, 1, 159-170

[14] Pentland, A.P., A new sense for depth of field, IEEE Transactions of Pattern Analysis and Machine Intelligence, 1987, **PAMI**-9, 4, 523-531

[15] Savakis, A.E., and Trussell, H.J., Blur identification by residual spectral matching, IEEE T. Image Process, 1993, **2**, 2, 141-151

[16] Boyd, J.P., Asymptotic Coefficients of Hermite Function Series, J. Comput. Phys., 1984, **54**, 382-410

[17] Cooley, J.W., and Tukey, J.W., An algorithm for the machine calculation of complex Fourier series, Math. Comput., 1965, **19**, 297–301

[18] Verbeek, P.W., and van Vliet, L.J., On the location error of curved edges in low-passed filtered 2-D and 3-D images, IEEE T. Pattern Anal., 1994, **16**, 7, 726-733

[19] Emiris, I.Z., and Tzoumas, G.M., Algebraic study of the appolonius circle of three ellipses, EWCG, Eindhoven, March 9-11 2005

[20] Shmakov, S.L., A universal method of solving quartic equations, Int. J. Pure Appl. Math., 2011, **71**, 2, 251-259

[21] Watson, G. N., A treatise on the theory of Bessel functions, 1992, Cambridge University Press, 396

[22] Lucas, S.K., Evaluating infinite integrals involving products of Bessel functions of arbitrary order, J. Comput. Appl. Math., 1995, **64**, 269-282

[23] Westerweel, J., Effect of sensor geometry on the performance of PIV interrogation, Proc. 9th Int. Symp. Appl. Laser Tech. to Fluid Mech., 1998, 1.2.1-8

[24] Unser, M., Aldroubi, A., and Eden, M., B-spline signal processing: part II-efficient design and applications, IEEE Transactions on Signal Processing, **41**-2, 834-848

Figures

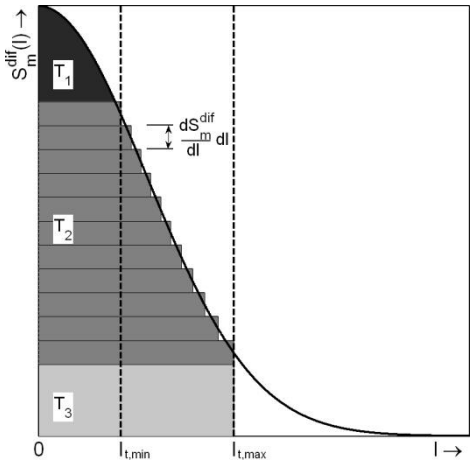

Fig. 1: Equivalence of convolution with $S_m^{dif}(l)$, assumed to be normally distributed, as a summation of concentric cylinders as expressed in (18). The minimum and maximum radius of the tangent circles are denoted by $l_{t,min}$ and $l_{t,max}$.

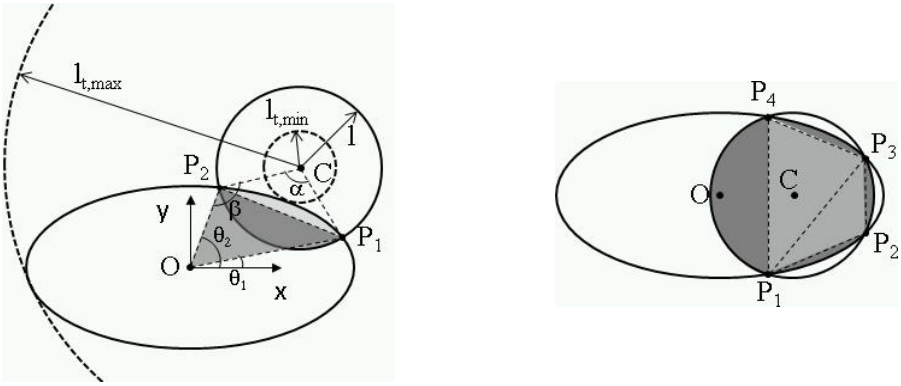

(a) (b)

Fig. 2: Parameter definition in ellipse circle overlap area in case of (a) two and (b) four intersection points.

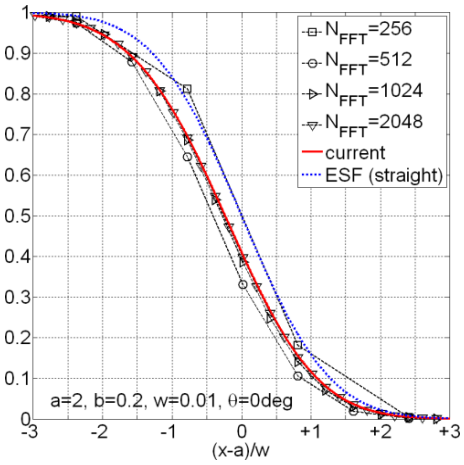

Fig. 3: Generic radial edge intensity profile along the ellipse semi-major axis as obtained by FFT evaluation of (9) for varying sampling frequency.

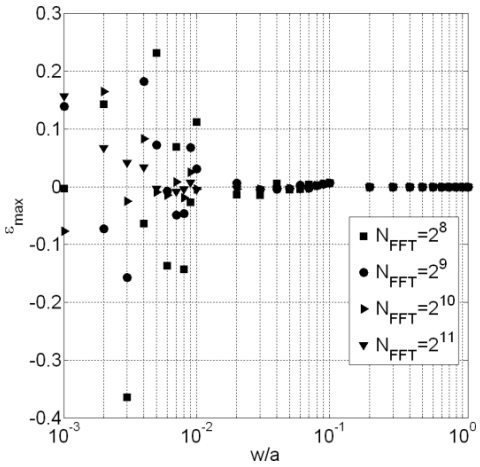

Fig. 4: Evolution of maximum discrepancy between FFT-based intensity profiles and proposed methodology with varying diffraction spot diameter and sampling points.

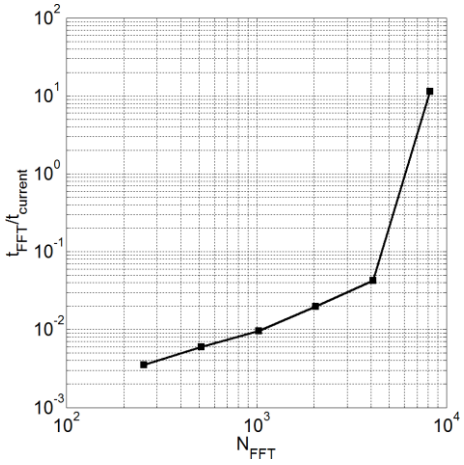

Fig. 5: Evolution in computation time ratio between FFT-based intensity reconstruction and the current convolution-based method with number of samples considered (both methods apply the same number of points).

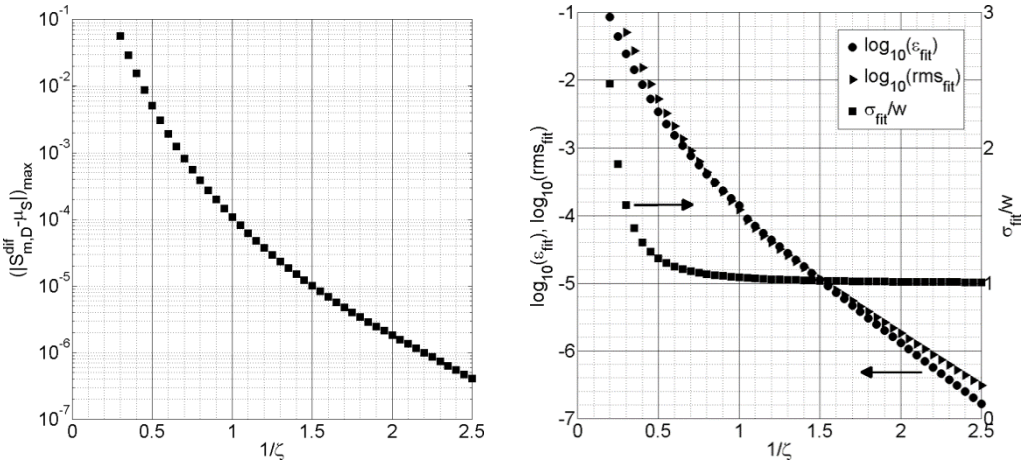

(a) (b)

Fig. 6: (a) Evolution of maximum normalised angular variation in $S_{m,D}^{dif}$ and (b) fitting error in function of $\zeta^{-1}=w/p\Delta$.

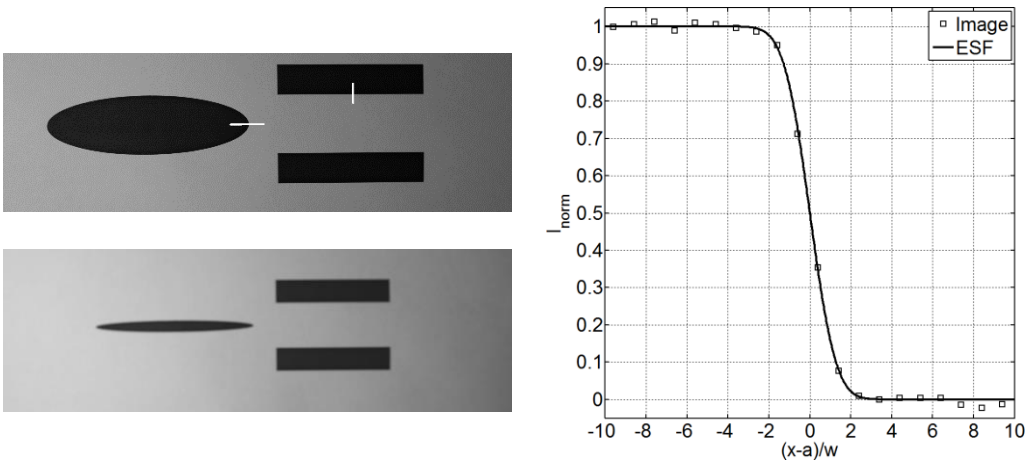

(a) (b)

Fig. 7: (a) Test images of ellipses to assess the suitability of the proposed intensity model - Top - *b/a=0.286*, *w/a=0.00213*. White lines indicate the profile extraction locations - Bottom - *b/a=0.0714*, *w/a=0.00986* (b) Analytical and measured ESF from the ellipse depicted in (a)-Top.

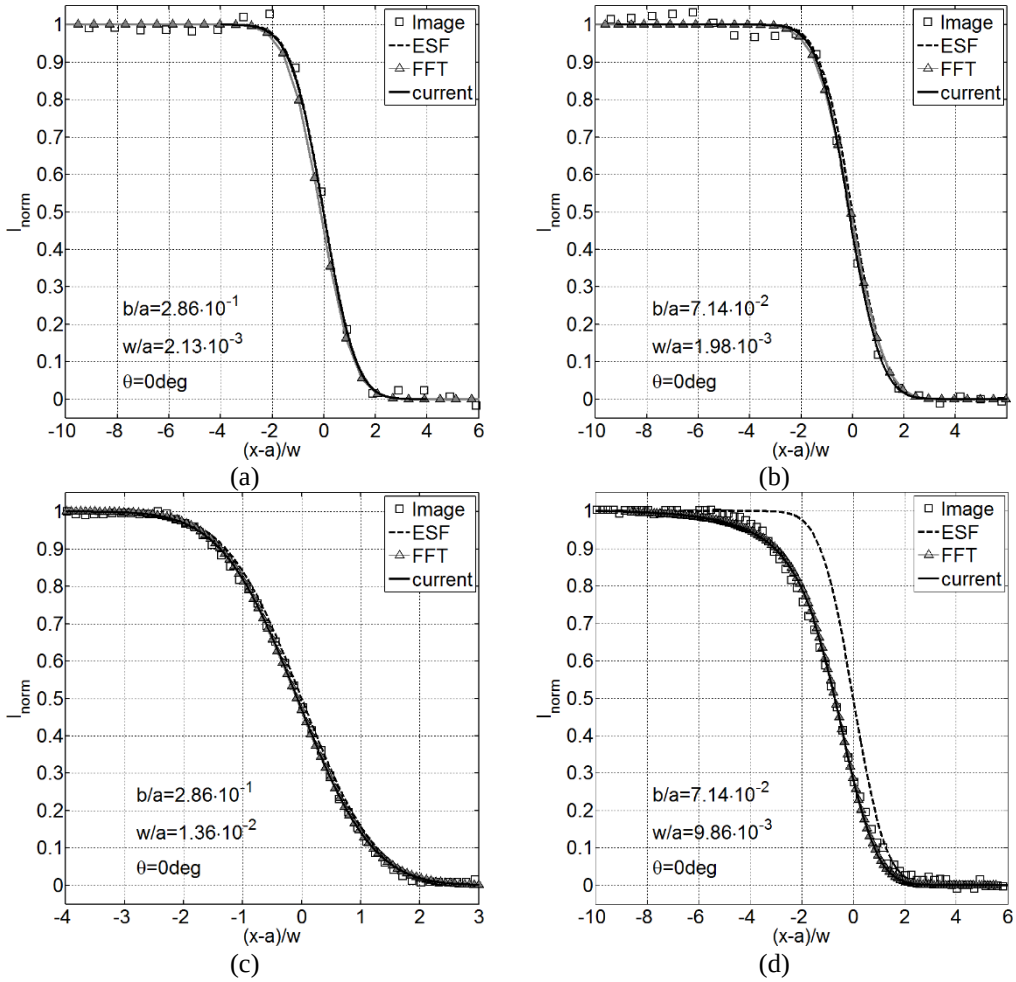

Fig. 8: Measured and simulated intensity profiles across the ellipse major semi-axis as obtained from the analytical ESF (17), FFT-based analysis (N_{FFT}=2048) and new proposed method. Thicker ellipse (a) in-focus (cf. Fig.7(a)-Top) and (c) out-of-focus. Thinner profile (b) in-focus and (d) out-of-focus (cf. Fig.7(a)-Bottom).